Received: 13 November 2018 | Revised: 1 February 2019 | Accepted: 11 February 2019

DOI: 10.1002/mrm.27725

FULL PAPER

Magnetic Resonance in Medicine

NMR shutter-speed elucidates apparent population inversion of ^1H_2O signals due to active transmembrane water cycling

Xin Li[1] | **Silvia Mangia**[2] | **Jing-Huei Lee**[3] | **Ruiliang Bai**[4] | **Charles S. Springer Jr**[1]

[1]Advanced Imaging Research Center, Oregon Health & Science University, Portland, Oregon

[2]Center for Magnetic Resonance Research, University of Minnesota, Minneapolis, Minnesota

[3]Department of Biomedical Engineering, University of Cincinnati, Cincinnati, Ohio

[4]Interdisciplinary Institute of Neuroscience and Technology, Qiushi Academy for Advanced Studies, Key Laboratory of Biomedical Engineering of Ministry of Education, College of Biomedical Engineering and Instrument Science, Zhejiang University, Hangzhou, China

Correspondence
Charles S. Springer, Jr., Advanced Imaging Research Center, Oregon Health & Science University, 3181 S.W. Sam Jackson Park Road, Mail code: L452, Portland, OR, 97239-3098.
Email: springer@ohsu.edu

Funding information
Brenden-Colsen Center for Pancreatic Care; Advanced Imaging Research Center

Purpose: The desire to quantitatively discriminate the extra- and intracellular tissue ^1H_2O MR signals has gone hand-in-hand with the continual, historic increase in MRI instrument magnetic field strength [$\mathbf{B}_0$]. However, recent studies have indicated extremely valuable, novel metabolic information can be readily accessible at ultra–low $\mathbf{B}_0$. The two signals can be distinguished, and the homeostatic activity of the cell membrane sodium/potassium pump (Na^+,K^+,ATPase) detected. The mechanism allowing ^1H_2O MRI to do this is the newly discovered active transmembrane water cycling (AWC) phenomenon, which we found using paramagnetic extracellular contrast agents at clinical $\mathbf{B}_0$ values. AWC is important because Na^+,K^+,ATPase can be considered biology's most vital enzyme, and its in vivo steady-state activity has not before been measurable, let alone amenable to mapping with high spatial resolution. Recent reports indicate AWC correlates with neuronal firing rate, with malignant tumor metastatic potential, and inversely with cellular reducing equivalent fraction. We wish to systematize the ways AWC can be precisely measured.

Methods: We present a theoretical longitudinal relaxation analysis of considerable scope: it spans the low- and high–field situations.

Results: We show the NMR shutter-speed organizing principle is pivotal in understanding how trans–membrane steady–state water exchange kinetics are manifest throughout the range. Our findings illuminate an aspect, apparent population inversion, which is crucial in understanding ultra-low field results.

Conclusions: Without an appreciation of apparent population inversion, significant misinterpretations of future data are likely. These could have unfortunate diagnostic consequences.

KEYWORDS
active water cycling, apparent population-inversion, shutter-speed

1 | INTRODUCTION

1.1 | Discerning tissue water compartmentalization

The major water compartmentalization in tissue is intra- and extracellular ("inside"/"outside"). In almost all parenchymal tissue, the vascular space comprises a small volume fraction. Thus, in the simplest approximation, this is a *two site* situation. A reliable way to quantitatively discriminate in vivo $^1H_2O_i$ and $^1H_2O_o$ NMR signals has been a very long quest.

1.2 | Active transmembrane water cycling

Recently, this pursuit has gained much greater importance. It has been discovered that the pseudo-first-order rate constant for *homeostatic* cellular water efflux (k_{io}) has an energetically active component, $k_{io}(a)$, as expressed in Equation 1, and

$$k_{io} = k_{io}(p) + k_{io}(a) \tag{1}$$

elaborated in Equation 2. The passive component, $k_{io}(p)$, is $\langle A/V\rangle P_W(p)$, where: $\langle A/V\rangle$ represents

$$k_{io} = \langle \frac{A}{V} \rangle P_W(p) + \left(\frac{x}{[H_2O_i]\ \langle V\rangle} \right) {}^cMR_{NKA} \tag{2}$$

the voxel average or region of interest average ⟨cell surface area/volume⟩ ratio, and $P_W(p)$ is the diffusive ("passive") cell membrane water permeability coefficient. In this study, quantities in brackets, ⟨⟩, represent voxel or region of interest averages. All symbols and acronyms are defined in the Appendix. It was previously thought $k_{io} = k_{io}(p)$: there was no active component. However, this is not the case: $k_{io}(a)$ is always present, and often dominant.[1-4] It is elaborated as $(x/([H_2O_i]\langle V\rangle))^cMR_{NKA}$, where $^cMR_{NKA}$ is the cellular metabolic rate of the cell membrane Na^+,K^+-ATPase (NKA) (fmol(ATP)hydrolyzed/cell/s), $[H_2O_i]$ is the intracellular water concentration, and x is the stoichiometric mole ratio of water actively cycled to ATP hydrolyzed by NKA [fmol(H_2O)/fmol(ATP)]. Thus, an enzymatic activity generates a membrane permeability. Active transmembrane water cycling (AWC) is a fundamental aspect of water biology not previously described.

This is important because NKA can be considered biology's most vital enzyme, but its in vivo homeostatic activity has never been measurable or amenable to mapping.[1-4] Significantly, it has been found that k_{io} correlates with metastatic potential in breast[5] and melanoma[6] cell lines, and with neuronal firing in brain tissue.[4] This is a new imaging biomarker with potentially great power.

Previously, the main candidate techniques for $^1H_2O_i/^1H_2O_o$ signal discrimination required the use of an exogenous, extracellular paramagnetic contrast agent (CA_o) to increase the $^1H_2O_o$ R_{1o} ($\equiv 1/T_{1o}$) value selectively.[3,7,8] This will be detailed below. Indeed, studies on model systems,[1-4,9,10] in which constant $[CA_o] \geq 5$ mM can be sustained during complete relaxation recovery measurement, were required to confirm the $(x/([H_2O_i]\langle V\rangle))^cMR_{NKA}$ term in Equation 2. However, this approach is problematic for in vivo human study.[3]

Since the beginning of NMR, there has been a seemingly inexorable march to instruments with higher magnetic field ($\mathbf{B}_0$) values.[11] This has been driven by the increased signal/noise ratio and spectral dispersion. However, this trend has not been particularly helpful for the discrimination of $^1H_2O_i$ and $^1H_2O_o$. Even though CA detectability increases slightly with increasing $\mathbf{B}_0$,[12] the diminished relaxivity (r_1) of approved CAs at current clinical $\mathbf{B}_0$ values[13] requires large CA doses. Consequently, safety and environmental regulatory restrictions preclude achieving the high, sustained $[CA_o]$ values sufficient for precise k_{io} determination in vivo.[3] Recently, Aime and co-workers have demonstrated CA-free $^1H_2O_i/^1H_2O_o$ discrimination, again in an animal model and cell suspensions, at ultra-low $\mathbf{B}_0$ values.[5,10] Here, we present a comprehensive analysis of the fundamental principles spanning the high and low field experiments.

2 | METHODS

2.1 | Intrinsic sample or voxel compartmental properties

There are two *intrinsic* NMR properties of interest: R_{1i} and R_{1o}, R_{1i} is the $^1H_2O_i$ R_1 value. For CA-enhanced MRI, the $^1H_2O_o$ R_1 value is given by Equation 3,

$$R_{1o} = r_{1o}\left[CA_o\right] + R_{1o0} \tag{3}$$

where r_{1o} is the extracellular CA longitudinal relaxivity $[CA_o]$, the extracellular CA concentration, and R_{1o0} the R_{1o} value in the absence of CA. In addition to being temperature–dependent, the R_{1i}, r_{1o}, and R_{1o0} properties are also $\mathbf{B}_0$–dependent.

There are two *intrinsic* cell biology properties of interest: p_i, and k_{io}. The quantity p_i is the mole fraction ("population") of water that is intracellular. The intracellular volume fraction, v_i, is given by Equation 4, where f_M is

$$v_i = (1 - f_M)\, p_i + f_M \tag{4}$$

the tissue volume fraction inaccessible to mobile aqueous solutes.[2,8] When the vascular fraction is neglected, Equations 5a and 5b obtain, where p_o and v_o are the respective extracellular mole and volume fractions.

$$p_o = 1 - p_i \tag{5a}$$

$$v_o = 1 - v_i. \tag{5b}$$

The pseudo-first-order rate constant for homeostatic cellular water efflux is k_{io}. (The parameter k_{io} is the reciprocal of the mean intracellular water molecule lifetime, $1/\tau_i$. The τ_i value is often reported in the literature.) Because we assume a steady-state, k_{io} is also given by Equation 6, where k_{oi} is the corresponding influx rate constant. While still

$$k_{io} = (p_o/p_i)\, k_{oi} \tag{6}$$

temperature-dependent, p_i, f_M, k_{io}, and k_{oi} do *not* depend on $\mathbf{B}_0$ or $[CA_o]$.

Figure 1 illustrates the isothermal behavior of realistic, representative intrinsic NMR properties over a very large range. The ordinate measures R_1: the R_{1i} curves are blue, while the R_{1o} curves are red. The abscissa is bifurcated: the left side measures an increase in log ν_L, the Larmor resonance frequency (proportional to log $\mathbf{B}_0$: the ^{1}H magnetogyric ratio is 0.023 T/MHz), with $[CA_o] = 0$; while the right side measures an increase in $[CA_o]$, with ν_L constant at 43 MHz ($\mathbf{B}_0 = 1.0$ T), the largest ν_L reached on the left. The smooth R_{1i} and

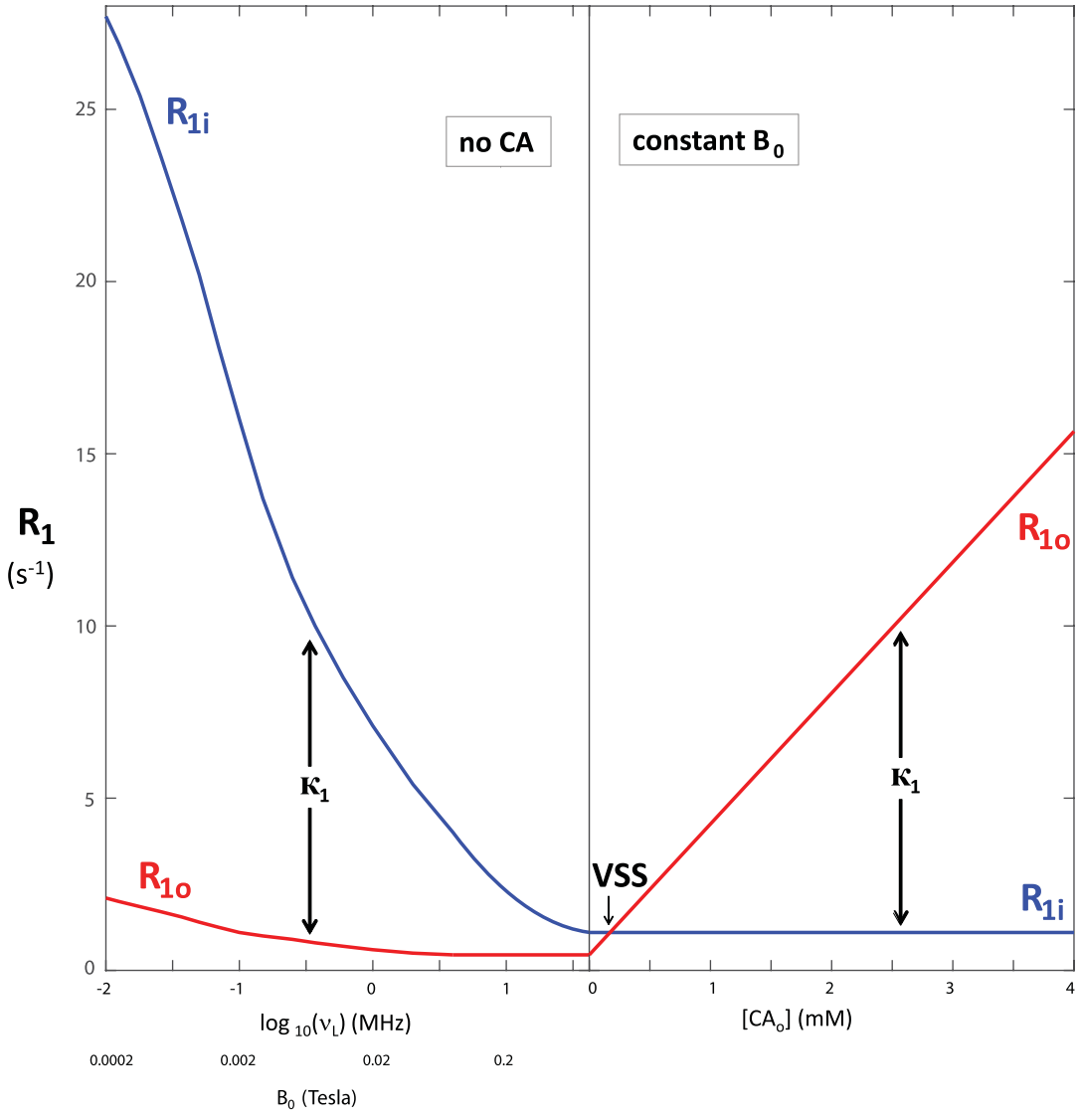

FIGURE 1 The dependences of the stipulated *intrinsic* compartmental longitudinal relaxation rate constants, R_1, on the: magnetic field, $\mathbf{B}_0$ (left), and extracellular CA concentration, $[CA_o]$ (right). The left abscissa has a log $\mathbf{B}_0$ scale, with fixed $[CA_o] = 0$. The right abscissa is linear in $[CA_o]$, with fixed $\mathbf{B}_0 = 1.0$ T. The intracellular R_{1i} (blue) and extracellular R_{1o} (red) rate constants on the left include those reported in Ruggiero et al.[5] The R_{1o} values on the right were calculated from Equation 3 with extracellular CA relaxivity, $r_{1o} = 3.8$ mM^{-1}s^{-1}. The longitudinal MR shutter–speed, κ_1 (Equation 9), and the VSS condition are indicated. It is important to note these would be the experimentally measured R_1 rate constants if there was no trans-cytolemmal water exchange [k = 0]

R_{1o} curves on the left pass through fitted values for a murine xenograft TS/A breast cancer tumor.[5] They exhibit the familiar dispersive shape [an R_{1i} inflection point near 0.1 MHz (0.002 T)]. The R_1 $\mathbf{B}_0$-dependence has long been referred to as NMR dispersion. The R_{1o} values on the right are calculated using $r_{1o} = 3.8\ s^{-1}(mM)^{-1}$, typical for approved Gd(III) chelates.[7] All magnitudes are for T = 37°C.

Figure 2 illustrates the behavior of the intrinsic cell biology properties: we take representative values of p_i (0.8) and k_{io} (1 s^{-1}).[3,5] (Thus, $p_o = 0.2$, and $k_{oi} = 4\ s^{-1}$ [$k_{io} + k_{oi} = 5\ s^{-1}$]). The left ordinate measures the p values (p_i, blue; p_o, red), while the right ordinate measures the overall exchange rate constant, k, given by Equation 7. The abscissa is

$$k = k_{io} + k_{oi} \tag{7}$$

the same as for Figure 1. Because these are isothermal plots, these properties exhibit horizontal lines.

2.2 | Magnetic field-dependence

It has long been known the tissue ^1H_2O R'_1 (the observed, approximated monoexponential R_1 value) increases with decreasing $\mathbf{B}_0$ (reviewed in Rooney et al[11]). In the absence of CA_o, the ^1H_2O longitudinal relaxation mechanism is generally dominated by water intramolecular $^1H - {}^1H$ magnetic dipole fluctuations at the ν_L frequency. As $\mathbf{B}_0$ decreases, the ν_L value decreases toward the increased probability of experiencing such fluctuations ("spectral density") found in tissue.[14] In contrast, the ^1H_2O R_1 value of pure water is not very $\mathbf{B}_0$–dependent: the inherent fluctuations have much greater frequency [reciprocal of the molecular rotational ("tumbling") correlation time constant, $\tau_r^{-1} \cong 10^{12}\ s^{-1}$] than ν_L, and thus are too fast for efficient relaxation.[11,14] Therefore, it has long been suspected the inverse R_1, ν_L relationship is due to the presence of macromolecules in tissue. Macromolecular tumbling is much slower than that of the molecules in pure water.[15] The fluctuation is $\tau_r^{-1} \cong 1.7/MW$, where MW is the macromolecular mass in kDa. (Thus, even a smallish 100 kDa macromolecule has $\tau_r^{-1} \cong 1.7 \times 10^7\ s^{-1}$.) To our knowledge, there is no simple physical model that predicts the $\mathbf{B}_0$-dependence of tissue ^1H_2O R'_1. Any attempt to match data with, say, a superposition of Lorentzian functions requires an empirical distribution of τ_r values.[11]

The extra- and intracellular tissue spaces both contain macromolecules,[3] and one could not know for certain if extra- or intracellular macromolecules, or both, dominated the effect. One avoids this uncertainty by writing Equation 8 for iron-free tissue.[11] In this expression: r_{1M} is the tissue macromolecular relaxivity, and R_{1H2O} is

$$R'_1 = r_{1M} f_M + R_{1H2O} \tag{8}$$

the pure water R_1 at physiological temperature. (An extra term can be added if a tissue contains a sufficient amount of paramagnetic iron.[11]) The greater r_{1M} decrease with *increasing* $\mathbf{B}_0$ compared with that of r_{1o} is the cause of the aforementioned slight CA detectability increase.[12]

However, Ruggiero and co-workers used a Matrigel phantom as a model for extracellular space.[5] They found the R_{1o}

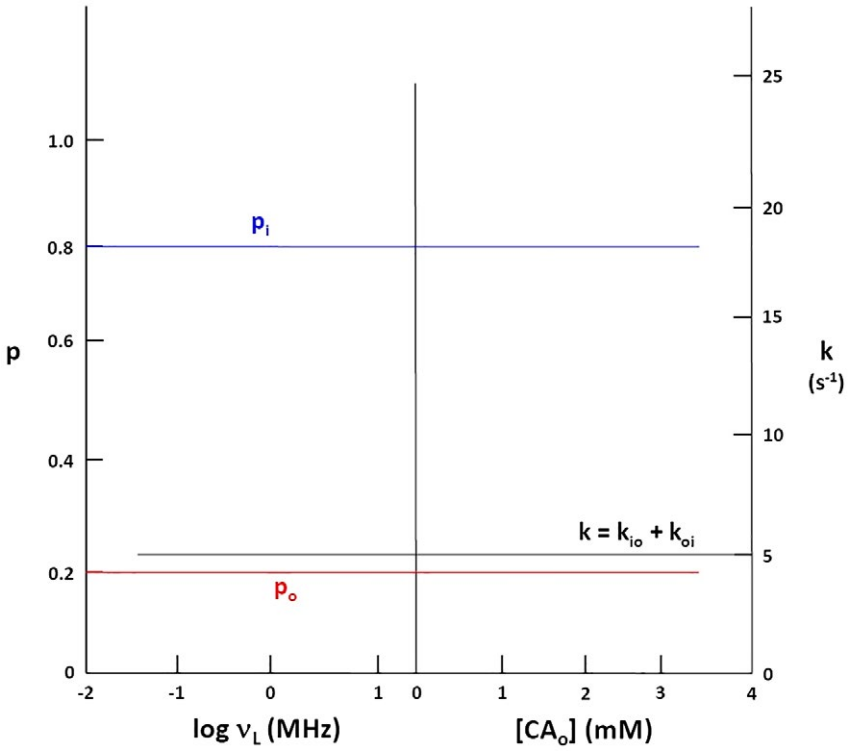

FIGURE 2 The non-dependences of the stipulated *intrinsic* compartmental mole fractions ("populations"), p, and intercompartmental exchange rate constant, k (Equation 7), on: (left) the $\mathbf{B}_0$ and (right) the [CA_o]. The abscissa is the same as in Figure 1. The intracellular p_i (blue) and extracellular p_o (red) populations are measured on the left ordinate, while k is measured on the right ordinate

value, so approximated, exhibits only a very slight NMR dispersion, as seen in Figure 1 (left). This supports a long-held suspicion that the R'_1 $\mathbf{B}_0$-dependence is dominated by an increasing R_{1i} value with decreasing $\mathbf{B}_0$.[16] This is attributed to sites for water molecules that are characterized as "buried" within macromolecules (H_2O_{bu}), and the surmise that such sites are more abundant in intracellular than in extracellular macromolecules.[16] Water molecules in such sites can more fully experience the slower macromolecule rotation, and thus particularly effective slow intramolecular $^1H - {}^1H$ fluctuations. Such macromolecules are endogenous, intracellular contrast agents, CA_is. Although their concentrations do not increase with decreasing $\mathbf{B}_0$, their relaxivities do. (Relaxivities and concentrations always appear together as products,[2,17,18] as in Equation 3.) Nonetheless, the miniscule number of H_2O_{bu} molecules are still in rapid exchange (rate constant > 10^4 s^{-1})[19] with the vastly greater number of all other H_2O_i molecules, certainly as compared with the k_{io} magnitude. They could even use the Grotthuss proton hopping mechanism.[15] In any case, the cytoplasm is "well–mixed." This is depicted in the Figure 3 cartoon. Some very large heterogeneous compartments (e.g., *Xenopus* oocyte [$\langle V \rangle$ = 840 nL] cytoplasms)[20] can exhibit inhomogeneous ^1H_2O resonances. However, most tissue cell $\langle V \rangle$ values range from hundreds of fL to a few pL.[21] In such small cells, even a conservatively small diffusion coefficient leads to good water mixing in any NMR experimental time period.[9]

The steady-state transmembrane water molecule exchange process, $k = k_{io} + k_{oi}$, is rate-limiting; i.e., slower than essentially all other water molecule interaction kinetics in tissue. And, this has been the source of considerable confusion in the in vivo MRI literature. If the exchange kinetics were exceedingly slow, or exceedingly fast, the interpretation of experimental ^1H_2O R'_1 data would be straightforward. But slow and fast are rather misleading adjectives. Figure 2 shows the k does not depend on $\mathbf{B}_0$ or $[CA_o]$. This is why we introduced[18] the concept of the longitudinal NMR relaxation shutter-speed, κ_1,[3,8] the absolute value function defined in Equation 9. The comparison of k with κ_1

$$\kappa_1 \equiv |R_{1i} - R_{1o}| \tag{9}$$

determines the "exchange condition" of the tissue ^1H_2O MR signal. If k is insufficiently greater than κ_1, a "slow" condition obtains: but if it is sufficiently larger, the system is in a "fast" condition. In experimental terms, a slow condition means the longitudinal relaxation is non-monoexponential, and a fast condition means the relaxation is monoexponential. The k_{io} measurement precision depends on the extent κ_1 exceeds k. Obviously, the greater the k value, the larger the κ_1 required.

As Figures 1 and 4 indicate, in biological tissue it is κ_1 that can be manipulated by the investigator [by means of $\mathbf{B}_0$ and/or $[CA_o]$], usually not k (almost all in vivo studies are isothermal). Because k does not change, the exchange reaction does not go "faster" or "slower." Using these terms is meaningful only if one thinks of κ_1 changes as "warping" time. Thus, a slow condition is more profitably understood as a "large-shutter-speed" (LSS) condition; and a fast condition as a "small-shutter-speed" (SSS) condition. These distinctions are important because the nature of the exchange condition strongly influences the correct interpretation of the experimental result. This is described by the well-known Bloch–McConnell-Woessner (BMW) Rate Law Equations[18,22,23], which elaborate the phenomenological signal equation.

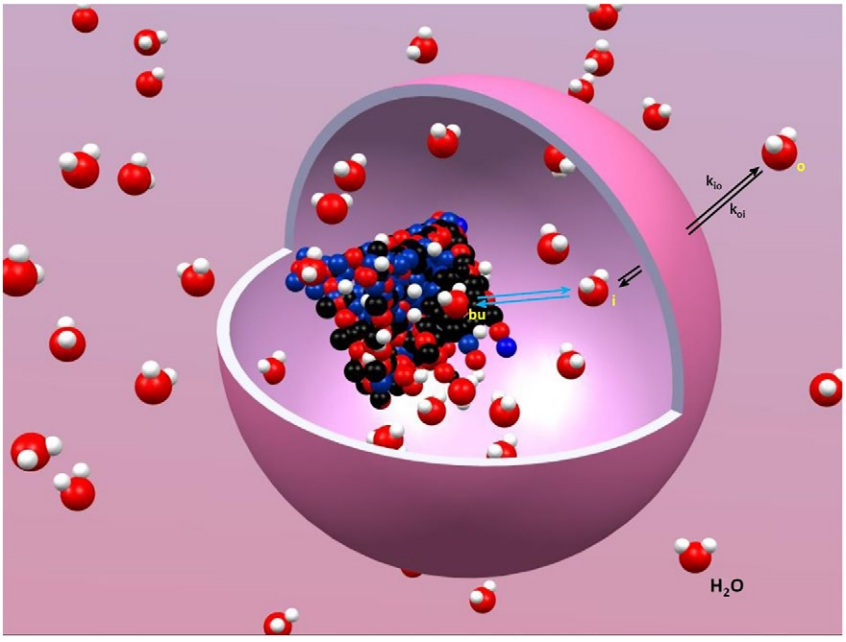

FIGURE 3 A stylized cartoon depiction of the steady-state water exchange processes that dominate the tissue ^1H_2O MR signal longitudinal relaxation at ultra-low-field. The trans-cytolemmal process has a k_{io} (Equation 2) and a k_{oi} (Equation 6) rate constants. The exchange of water out of and into macromolecular buried sites, H_2O_{bu}, is much faster than $k = k_{io} + k_{oi}$. For the considerations here, cytoplasmic water is "well-mixed." This figure was prepared with the help of Gangxu Han

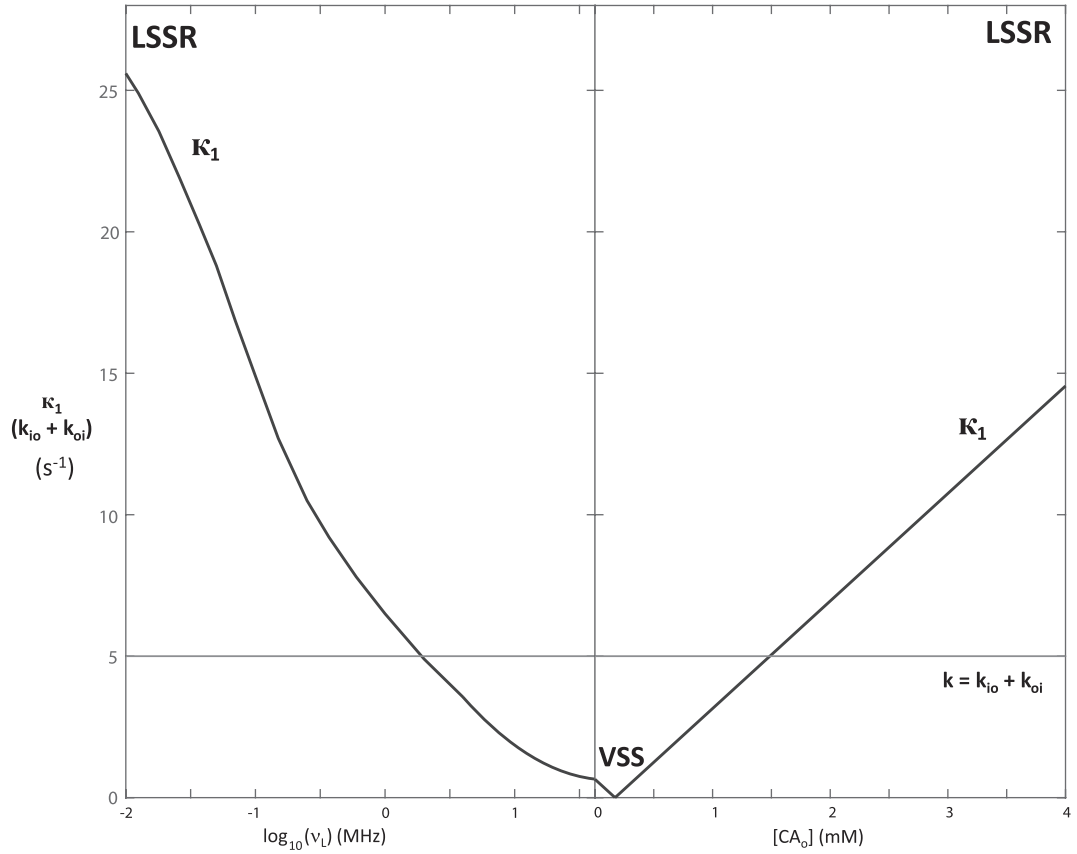

FIGURE 4 The dependences of the stipulated MR shutter-speed, κ_1 (Equation 9), and intercompartmental exchange rate constant, k (Equation 7), on (left) the $\mathbf{B}_0$ and (right) the $[CA_o]$. The abscissa is the same as in Figure 1, and the ordinate the same as on the right in Figure 2. The vanished shutter-speed VSS condition is indicated. The rate constant k_{io} can be determined with precision only when $\kappa_1 >> k$, the large shutter-speed regime LSSR period

2.2.1 | Apparent sample or voxel compartmental properties

The experimental relaxation decay is often fitted with an *empirical* bi–exponential expression, with *apparent* fast and slowly relaxing components that are not coupled by molecular exchange, Equation 10, where: S can be a recovery time-course signal or a multi-pulse MR steady-state

$$S/S_0 = p'_{fast}\,\mathbf{S}'_{fast} + p'_{slow}\,\mathbf{S}'_{slow} \tag{10}$$

signal, S_0 is the Boltzmann signal, p'_{fast} and p'_{slow} the apparent populations, and $\mathbf{S}'_{fast}$ and $\mathbf{S}'_{slow}$ are fractional recovery or longitudinal and transverse relaxation saturation factor functions (running from 1 to 0). When transverse relaxation cannot be ignored, the saturation factor functions can be complicated. These are left implicit in Equations 11 and 12,

$$\mathbf{S}'_{fast} = f\left(time, \alpha, TR, R'_{1,fast}, TE, R'_{2,fast}\right) \tag{11}$$

$$\mathbf{S}'_{slow} = f\left(time, \alpha, TR, R'_{1,slow}, TE, R'_{2,slow}\right) \tag{12}$$

where time is the recovery period, and α, TR, and TE are the steady-state acquisition pulse flip angle, repetition time, and echo time, respectively. (We have presented examples of recovery[2,9] and longitudinal steady-state[7] functions.) Each apparent component is defined to have single R'_1 ($R'_{1,fast}$, $R'_{1,slow}$) and complicated R'_2 ($R'_{2,fast}$, $R'_{2,slow}$) values.

However, in the vast majority of in vivo MR experiments, there is molecular exchange (steady–state) between the populations, and this makes the situation completely different from the empirical bi–exponential description. This is true even if, to simplify the subsequent derivation, we set $\mathbf{S}'_{fast} = \mathbf{S}'_{slow} = 1$. (As we will see below, however, this is probably, and importantly, not true for in vivo experiments, where multipulse acquisition, with incomplete recovery, is required for imaging purposes.) For nonimaging studies of model systems, S can be measured with $\alpha = 90°$ and complete recovery (large TR). Thus, the longitudinal saturation components in Equations 11 and 12 can be dealt with.

With these caveats, the *apparent* longitudinal relaxation rate constants, R_1', and longitudinally "fully relaxed" ("unsaturated") *apparent* mole fractions, p′, are expressed, in the isochronous ($\nu_{Lo} = \nu_{Li}$) BMW two-site-exchange (2SX) exchange Equations 13 through 16, as functions of the *intrinsic* system parameters.[7,18,22,23]

$$R'_{1,fast} = \frac{1}{2}\left[(R_{1i}+R_{1o})+k\right] + \frac{1}{2}\left\{\left[(R_{1i}-R_{1o})+(k_{io}-k_{oi})\right]^2 + 4k_{io}k_{oi}\right\}^{1/2} \quad (13)$$

$$R'_{1,slow} = \frac{1}{2}\left[(R_{1i}+R_{1o})+k\right] - \frac{1}{2}\left\{\left[(R_{1i}-R_{1o})+(k_{io}-k_{oi})\right]^2 + 4k_{io}k_{oi}\right\}^{1/2} \quad (14)$$

$$p'_{fast} = \frac{1}{2} - \frac{1}{2}\left\{\frac{(R_{1i}-R_{1o})(p_o-p_i)+k}{\left\{\left[(R_{1i}-R_{1o})+(k_{io}-k_{oi})\right]^2 + 4k_{io}k_{oi}\right\}^{1/2}}\right\} \quad (15)$$

$$p'_{slow} = \frac{1}{2} + \frac{1}{2}\left\{\frac{(R_{1i}-R_{1o})(p_o-p_i)+k}{\left\{\left[(R_{1i}-R_{1o})+(k_{io}-k_{oi})\right]^2 + 4k_{io}k_{oi}\right\}^{1/2}}\right\}. \quad (16)$$

(These equations correct typographical errors in Equations 6 and 7 of Li et al.[7] The term that was printed as $p_i(1 - p_i)/\tau_i$ in Equation 6 should have been $p_i/[(1 - p_i)\tau_i]$, and the square root should have been of the Equation 7 denominator.) Each apparent parameter has contributions from *both* analogous intrinsic parameters.

3 | RESULTS

It is very important to recognize the experimentally measured relaxation rate constants and mole fractions (R_1' and p′) are not the same as the system R_1 and p values that are desired. We input the Figures 1 and 2 intrinsic parameter values into Equations 13-16 to "reverse engineer" typical parameters from experiments. This is illustrated in Figures 5 and 6, where expected R'_1 and p′ values, respectively, are plotted with abscissae identical to that of Figures 1, 2, and 4. The Figure 5 ordinate is identical to that of Figure 1, while the Figure 6 ordinate is identical to the Figure 2 left ordinate. The empirical labels are given outside the right ordinates: $R'_{1,fast}$ (Equation 13) and $R'_{1,slow}$ (Equation 14) for Figure 5, and p'_{slow} (Equation 16) and p'_{fast} (Equation 15) for Figure 6. In Figure 1, the R_{1i} and R_{1o} values cross (point): $R_{1,cross} = R_{1i} = R_{1o} = 1.1\ s^{-1}$ at $[CA_o] = 0.17$ mM. This would be the experimental result if there was no exchange: k = 0, the no-exchange-limit (NXL). However,

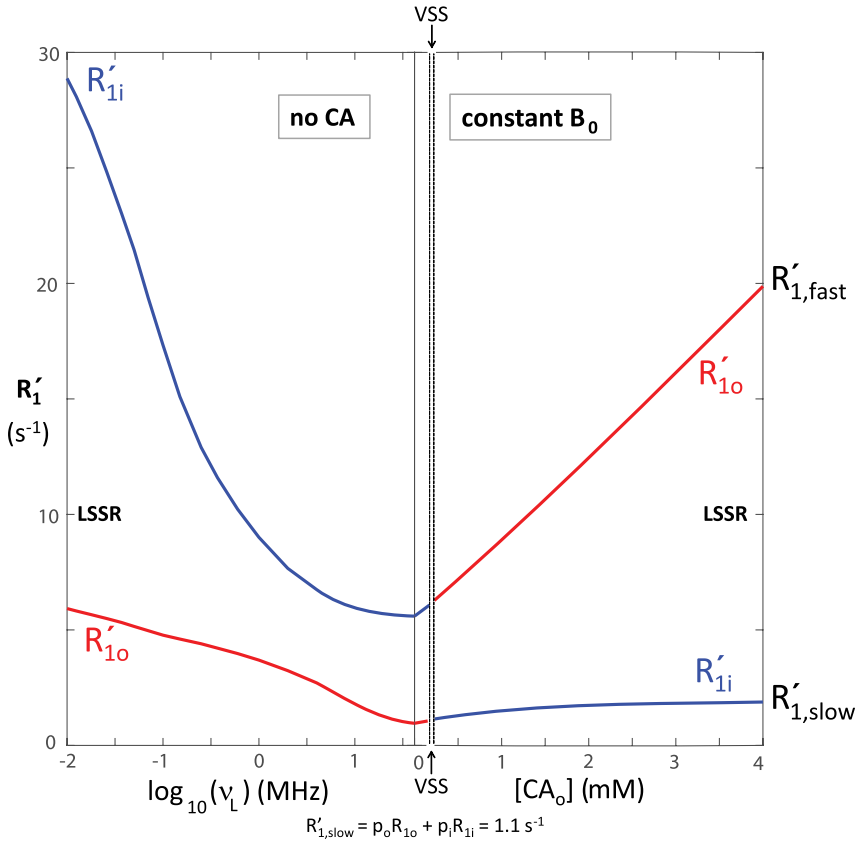

FIGURE 5 With the *intrinsic* parameters from Figures 1 and 2, we calculated the dependences of the expected *apparent* compartmental longitudinal relaxation rate constants, R'_1 ($R'_{1,fast}$, Equation 13; $R'_{1,slow}$, Equation 14) on (left) the $\mathbf{B}_0$ and (right) the $[CA_o]$. The R'_{1i} and R'_{1o} rate constant segments are colored blue and red, respectively. The colors switch when the curves pass through the VSS condition. The abscissa is the same as in Figure 1, and the ordinate the same as on the left in Figure 1

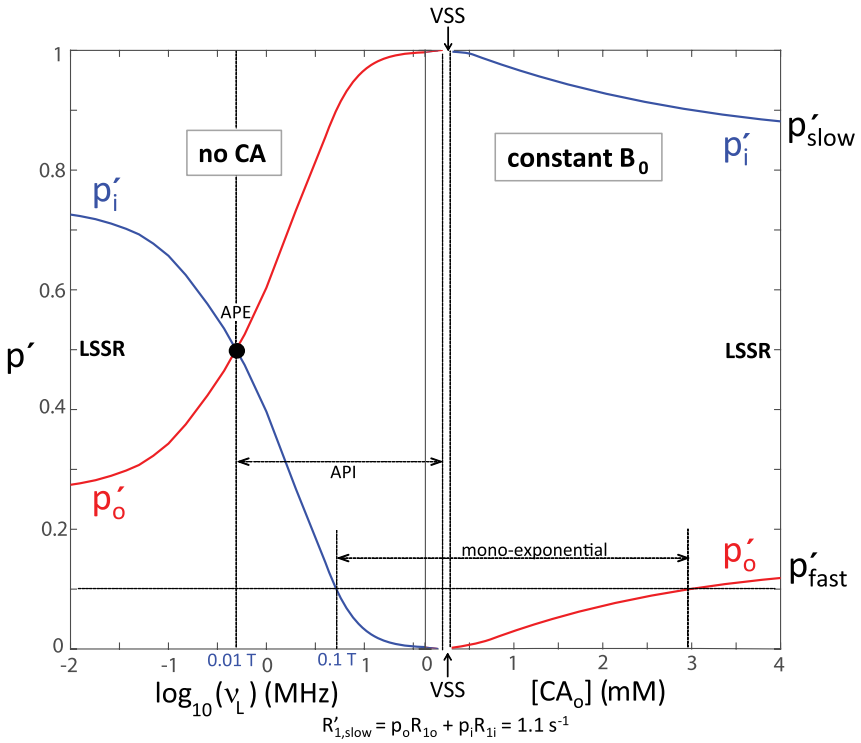

FIGURE 6 With the *intrinsic* parameters from Figures 1 and 2, we calculated the dependences of the expected (longitudinally) fully relaxed *apparent* compartmental populations, p′ (p'_{slow}, Equation 16; p'_{fast}, Equation 15) on (left) the $\mathbf{B}_0$ and (right) the $[CA_o]$. The p'_i and p'_o population segments are colored blue and red, respectively. The colors switch when the curves pass through the VSS condition. The abscissa is the same as in Figure 1, and the ordinate the same as on the left in Figure 2. An apparent population equality APE point is indicated, as is the region of apparent population inversion API, along with a conservatively small monoexponential relaxation regime. Unfortunately, current clinical MRI protocols fall within this latter region: the system is constrained to the vast shutter–speed "wasteland" exhibited in Figure 4

when exchange kinetics are finite this crossing is avoided (Figure 5). (See also Figure 3 of Bai et al[24] and Figure 4 of Labadie et al.[25]) This result is a property of the "mixing" inherent in any coupled differential equations, such as those giving rise to Equations 13-16.

At the smallest $\mathbf{B}_0$ (0.0002 T; $\nu_L = 0.01$ MHz) and largest $[CA_o]$ (4 mM) values simulated, when κ_1 is maximally different from k (Figure 4), the R'_{1i} and R'_{1o} values are just approaching the LSS limit (LSSL) condition ($\kappa_1 >> k$) values: $R'_{1,fast} = R_{1i} + k_{io}$ ($28 + 1 = 29\ s^{-1}$) on the left, and $R'_{1,fast} = R_{1o} + k_{oi}$ ($15 + 4 = 19\ s^{-1}$) on the right; $R'_{1,slow} = R_{1o} + k_{oi}$ ($2 + 4 = 6\ s^{-1}$) on the left, and $R'_{1,slow} = R_{1i} + k_{io}$ ($1 + 1 = 2\ s^{-1}$) on the right (Figure 5). However, more importantly, the p′ values (Figure 6) have clearly not yet reached the LSSL p′ values ($p_i = 0.8$, $p_o = 0.2$) (Figure 2). For in vivo human studies, it is currently not very practical to work near the earth's field (~0.0001 T),[26] and it is essentially disallowed to achieve $[CA_o]$ of even transiently 3 mM.[27] Thus, realistic clinical MR examinations are constrained to never even approach the LSSL condition. The shutter-speed cannot be increased sufficiently.

Therefore, one must account for steady-state transcytolemmal water exchange kinetics [k] if one wishes to extract accurate system p_i and p_o values. This has been experimentally demonstrated for myocardium,[28] where p_o (extracellular volume fraction, ECF) is an extremely important biomarker.[3] Changes in p_i and p_o report tissue edema (a *net* intercompartmental water transfer) because the mean cell volume $\langle V \rangle = v_i/\rho$, where ρ is the cell (number) density (*e.g.*, cells/μL): the relationship between v_i and p_i is given in Equation 4. Assuming either $k = \infty$ (as has frequently been done), or $k = 0$, is incorrect.

3.1 | Relaxation exponentiality

Figure 6 is very informative. It is unproductive to consider only the empirical $R'_{1,fast}$, $R'_{1,slow}$, p'_{slow}, and p'_{fast} parameters. What are important are the intrinsic parameters with which they correlate. Because we have simulated over such a wide range, we can assign segments of the apparent curves correctly (blue for R'_{1i} and p'_i; red for R'_{1o} and p'_o). When κ_1 approaches zero, the faster relaxing apparent component vanishes ($p'_{fast} \rightarrow 0$; Figure 3 of Bai et al,[24] Figure 2 of Vétek et al[29]), and the experimental relaxation time-course becomes monoexponential (R'_1 is single-valued). When κ_1 is actually zero, the vanished shutter-speed (VSS, Figures 1, 4-6) condition, R_1' is given by Equation 17.[30]

$$R'_1 = p_o R_{1o} + p_i R_{1i} = R_{1,cross}. \quad (17)$$

The signal arises from all the water: the k_{io} parameter does not enter the equation, and thus is intrinsically indeterminate.

Practically speaking, however, it is hard to experimentally detect a small minority component even when it is present. We draw a horizontal line at $p' = 0.1$ in Figure 6. It strikes the blue p'_i curve on the left at $\log \nu_L \cong 0.7$ ($\nu_L \cong 4.3$ MHz; $\mathbf{B}_0 \cong 0.1$ T), and the red p'_o curve on the right at $[CA_o] \cong 2.9$ mM. Because all current human MR instruments have $\mathbf{B}_0 > 0.1$ T and (as suggested above) $[CA_o]$ values > 3 mM cannot be sustained, clinical ^1H_2O data are constrained to exhibit apparent monoexponential longitudinal relaxation (single-valued R'_1). The accessible shutter speeds are too small (Figure 4): clinical MRI is trapped in a vast shutter-speed "wasteland." This regime indicated is conservatively small: it can be experimentally difficult to detect a minority component even with p' somewhat greater than 0.1.

To extract k_{io} and p_i when the relaxation is effectively monoexponential, when one is in the wasteland, one must *vary* $[CA_o]$ (as pharmacokinetically, after a bolus injection) or – now - $\mathbf{B}_0$, and take advantage, to the extent possible, of the nonlinear $R'_{1,slow}$ $[CA_o]$– or $\mathbf{B}_0$-dependence in this regime (Figure 5). Neglecting the p'_{fast} ($R'_{1,fast}$) contribution is the most common shutter–speed (dynamic-contrast-enhanced) DCE–MRI version [fast-exchange-regime-allowed (FXR-a)].[1,7,8,17,27,31] One can see (Figure 6) the p'_{fast} term is mostly vanished by the exchange effect. However, precision can be poor, and k_{io} indeterminate in circumstances of insufficient CA extravasation, negligibly small $[CA_o]$, as in the normal-appearing brain.[3]

We neglect potential non-monoexponential contributions from vascular H_2O or magnetization transfer (MT) from macromolecular ^1H resonances.[32] The model study systems are avascular, or effectively so. In vivo, the vascular contribution is generally limited to the initial portion of the DCE time-course.[8] Also, the low α, on–resonance RF pulse in a 3D imaging acquisition is generally not very MT sensitive.[33-35]

The contention that k_{io} can never be accessed by DCE-MRI is predicated on the supposed longitudinally fully relaxed p'_{fast} and p'_{slow} contributions.[36] The longitudinal saturation expressions (the α, TR, $R'_{1,fast}$, and $R'_{1,slow}$ functions of Equations 11 and 12 have been assessed (Figure S1 of Li et al[31]; Figure 6 of Buckley[36]). If not unity, these weight p'_{fast} disproportionately relative to p'_{slow}. (That is, they make $\mathbf{S}'_{fast}$ and $\mathbf{S}'_{slow}$ each less than unity, but $\mathbf{S}'_{fast} > \mathbf{S}'_{slow}$.) However, taking this into account and forcing data fittings with the fully longitudinally relaxed biexponential expressions (Equations 10-16) has been found to introduce unacceptable systematic errors, cause k_{io} to become artificially indeterminate,[7,31] and sometimes to make fittings poorer.[36] When the two components cannot be experimentally discriminated and separately fitted, the $R'_{1,fast}$ and $R'_{1,slow}$ $\mathbf{B}_0$- and $[CA_o]$-dependences tend to counteract one another (the "avoided crossing," Figure 5), and thus reduce k_{io} influence (Equations 13 and 14). It seems the p'_{slow} contribution is disproportionately (essentially *exclusively*) acquired. So, we consider the transverse saturation expressions (the TE, $R'_{2,fast}$, and $R'_{2,slow}$ functions of Equations 11 and 12). In DCE, TR is often < 5 ms, so TE must be very small. Although the saturation expressions can be very complicated,[33-35] an infinitely small TE is equivalent to $R'_{2,fast} = R'_{2,slow} = 0$. We have proposed, however, it is quite plausible that $R'_{2,fast}$ and $R'_{2,slow}$ are sufficiently nonzero due to magnetic susceptibility gradients.[7,31]

During the bolus CA passage, there are significant paramagnetic CA concentration gradients across capillary walls and cell membranes. Plasma [CA] can exceed 5 mM immediately upon CA arrival in the tissue.[27,36] Susceptibility gradients due to such concentration differences have been shown to significantly increase R'_2 values.[37] The fully relaxed p'_{fast} contribution has already been rendered much smaller than p'_{slow} by exchange (it vanishes in the VSS condition), Figure 6. Thus, even if $R'_{2,fast}$ and $R'_{2,slow}$ are equally elevated, it is easy to imagine the fortuitous consequence that p'_{fast} is completely saturated ("quenched"), leaving partially saturated p'_{slow} as the meaningful component. Whatever the mechanism, considerable experimental evidence has accumulated that k_{io} can be usefully estimated in many DCE–MRI experiments (see the Discussion section)

A truly noninvasive diffusion-weighted imaging (DWI) analysis that does not require a CA or a shutter–speed shows considerable promise in determining k_{io}.[3] This novel DWI approach works at clinical $\mathbf{B}_0$ values, seems to measure large k_{io} values with more precision, and allows separation of the irreducible v_i cell biology factors, ρ and $\langle V \rangle$. These pathology-related properties are very important in their own right, and in discriminating the 2 Equation two terms to access x^cMR_{NKA} itself: ρ and $\langle V \rangle$ are not accessible with DCE-MRI.[3]

3.2 | Apparent Population Inversion

Somewhere below 0.1 T, one can begin to detect non-monoexponential T_1 relaxation caused by k_{io}.[5,10] Figure 6 exhibits further interesting features. When the field value is small enough to observe apparent biexponential relaxation, but not yet as small as ~0.01 T, the apparent minority component does not extrapolate to the true minority component, p_o (red), but to the true majority component, p_i (blue). Between $\mathbf{B}_0 \cong 0.01$ T and the VSS, there is an apparent population inversion (API). This has been noted previously (Figure 4 of Lee and Springer[38]). If one conducts only an empirical biexponential analysis (Equations 10-12) of such experimental data, one would find the minority component (blue p' in Figure 6) has the faster relaxation (blue R'_1 in Figure 5). If the apparent minority p' value is near 0.2, as is quite likely, one would be tempted to incorrectly assign it to $^1H_2O_o$, or any population other than H_2O_i, because p_i is commonly understood to be

near 0.8. This is a common problem with the inappropriate application of an empirical biexponential analysis to data that do not have an intrinsic biexponential nature.[39] The condition of apparent population equality (APE) ($p_i' = p_o' = 0.5$; log $\nu_L \cong -0.35$ in Figure 6; $\nu_L = 0.43$ MHz, $\mathbf{B}_0 = 0.01$ T), and thus API, occurs only when the true majority component (p_i here) has the faster relaxation (R_{1i} on the left), and at the point given by Equation 18 (derived from Equations 15 and 16), where the κ_1 *argument* ($\arg\kappa_1$) is ($R_{1i} - R_{1o}$).

$$\arg \kappa_{1,APE} = k/(p_o - p_i). \tag{18}$$

4 | DISCUSSION

4.1 | Why does API happen?

The curves in Figures 5 and 6 are generated from the BMW 2SX Equations 13-16. On their RHSs, the shutter-speed argument ($R_{1i} - R_{1o}$) appears in many places, and it plays a pivotal role. It is the only factor that changes sign from the left to the right of Figures 5 and 6: being positive on the left, and negative on the right. As a consequence, it is always the population with the apparent faster relaxation that vanishes as the system approaches the VSS condition (two vertical dashed lines in Figures 5 and 6), which is where $\arg\kappa_1$ changes sign. This behavior can be seen graphically in simulated (Figure 3 of Lee and Springer[38]) and experimental (Figure S1 of Zhang et al[9]) decay curves, and can be derived from Equations 15 and 16. Thus, if the VSS is approached from the left in Figure 6, by increasing $\mathbf{B}_0$, it is p_i' that goes to zero. On the other hand, if the VSS is approached from the right, by decreasing [CA_o], it is p_o' that goes to zero. Our simulations here are all for $k = 5\ s^{-1}$. However, the rate of vanishing does depend on k: all other parameters held fixed, the greater the k the more shallow the vanishing.[24] As a corollary, when a system passes through the VSS condition, the assignments of the apparent relaxation rate constants ($\mathbf{R}'_1$s) and populations (p′s)

TABLE 1 k_{io} **Responsiveness to Metabolic Changes**

k_{io} increases with:	a	Increased NKA pump expression (5,9*)
	b	Increasing cytoplasmic ATP (9*)
	c	Increasing [K_o^+] (at low [K_o^+]), with an NKA Michaelis-Menten signature (4,43)
	d	Hypoxia (10,44#)
	e	Cisplatin-induced apoptosis (45)
	f	Xenograft tumor apoptotic regions (46#)
	g	Human brain metastasis radiosurgery (47#)
k_{io} decreases with:	h	Ouabain NKA pump inhibition (2,5,9*,43)
	i	Increasing [K_o^+] (at sufficient [K_o^+] to cause membrane depolarization) (4)
	j	WZB117 glucose uptake inhibition (5)
	k	$O_2 \rightarrow N_2$ switch (9*)
	l	Increasing mitochondrial reducing equivalents (6#)
	m	Intracellular lonidamine (48#) mitochondrial complex II inhibition (49)
	n	Extracellular tetrodotoxin voltage-gated sodium channel inhibition (4)
	o	Extracellular AP5 plus DNQX† post-excitatory neuronal activity inhibition (4)
	p	Glutamine deprivation (10)
	q	Hypertension in myocardium (28#)
	r	Chemotherapy of human breast tumors (50#)
	s	Phosphatase activation breast tumor therapy (51#)
k_{io} correlates with:	t	Tumor metastatic potential (5,6#)
	u	Neuronal firing (4)
	v	Oxidative phosphorylation rate (52&)
	w	O_2 consumption rate (4)
	x	Head and neck cancer mortality (53#)
	y	^{18}Fluoro-2-deoxy-D-glucose breast tumor uptake (54#)

ATP, adenosine triphosphate; k_{io}, water efflux k ($1/\tau_i$); NKA, Na^+,K^+-ATPase (sodium pump).

*For yeast, pump is PMA1, inhibitor is ebselen.

#Employed shutter-speed (κ_1) dynamic-contrast-enhanced-MRI.

†(2R)-Amino-5-phosphonovaleric acid plus 6,7-dinitroquinoxaline-2,3-dione.

&Indirect.

must be switched; from blue to red and vice versa in Figure 6. This can be observed in experimental data (Figure 3 of Zhang et al[40]).

The deviation of an observed p′ from its corresponding inherent compartmental p does have a physical basis. There are subcompartmental spin populations with different diffusion (phase diagram)[41] and/or exchange[31] histories. Thus, these can have different R_1 values, but surely they exist in continua.[42] Given these complications, the emphasis must remain on the *inherent* p values, which enjoy the well-mixed attribute, and these can be extracted only with 2SX analyses of experimental data. Furthermore, this is also the only way to determine k_{io} with a shutter–speed experiment.

4.2 | Implications

Many results indicate the new metabolic k_{io} biomarker can be very powerful. As befitting the crucial NKA role in intermediary metabolism, k_{io} has been reported responsive to several different metabolic alterations (Table 1). For instance, entries a, d, l, and t suggest that k_{io} reports from ground zero of the oncogenic transformation: it may increase because of the very ion transporter up–regulation that triggers K-Ras/rapidly accelerated fibrosarcoma kinase/mitogen-activated protein kinase signaled uncontrolled cell proliferation.[3] This suggests its potential for early cancer detection. These consequences are surely due to the ${}^{c}MR_{NKA}$ contribution to k_{io}(a). Because of its vital nature, ${}^{c}MR_{NKA}$ is likely to be altered in most, if not all, pathologies. Another example is systemic multiple sclerosis.[52] The Table 1 entries arising from DCE-MRI estimation are clearly marked with a superscript #. It is important to note that entries d and t show DCE-MRI results that have been validated with more precise ultra-low field model experiments not subject to the DCE uncertainties.

Damadian's early ex vivo 0.6 T ${}^{1}H_2O$ MR study to discriminate malignant and normal tissue[55] was cited by Lauterbur[56] as part of the motivation for developing MRI.[57] The fact that subsequent research showed sensitivity and specificity are insufficient for robust cancer detection has been one of the major drivers for the seemingly inexorable increase in $\mathbf{B}_0$ strength (moving to the right in the figures) in clinical MRI.[11,58] So, particularly the fact that Ruggiero and co-workers' results (although nonimaging) were obtained at very small $\mathbf{B}_0$ values, with a fast field cycling study (modest detection $\mathbf{B}_0$) of an in vivo murine xenographic tumor model,[5] will stimulate renewed interest in ultra–low field MRI (moving to the left in the figures). It is exciting to find AWC is the molecular process that dominates the ultra-low field ${}^{1}H_2O$ signal.

Ruggiero and co-workers' finding[5] that it is mainly the k_{io} increase with malignancy that leads to decreasing R'_1 provides an explanation for Damadian's classic observation of the latter phenomenon.[55] It suggests his ex vivo NMR acquisitions within five min of rat euthanasia were soon enough to retain most of the in vivo cellular ATP. Also, the increase of k_{io} with concomitant p_o increase in malignancy[5] is consistent with metabolic competition between cancer cells.[3] The greater the cell density, ρ, the slower the NKA activity per cell.

There has been only a small amount of fast field cycling work in human studies: a recent report at 0.06 T has been published.[59] However, significant efforts to produce such human-sized instruments are under way. The same is true for "portable" low-field scanners, with possibly $\mathbf{B}_0 < 0.1$ T (Garwood MG, personal communication).[60] These could become very valuable metabolic instruments.

Figure 6 illustrates, however, that $\mathbf{B}_0$ values sufficiently small to access the LSSL condition are quite unlikely to be reached. This emphasizes the importance of the BMW 2SX analysis detailed here. Otherwise, the bi–exponential relaxation results that will be obtained can be very easily miss–interpreted. This would cause quite unfortunate confusion, and actually represent a medical set–back.

ACKNOWLEDGMENTS

We thank Eric Baker, Thomas Barbara, Peter Basser, Michael Garwood, Erin Gilbert, Wei Huang, Shalom Michaeli, Martin Pike, William Rooney, Christopher Sotak, Lawrence Wald, Gregory Wilson, and Mark Woods for stimulating discussions, as well as Gangxu Han for Figure 3. X.L. and C.S.S. were supported in part by the *Brenden–Colson Center for Pancreatic Care* and the OHSU *Advanced Imaging Research Center*.

REFERENCES

1. Springer CS, Li X, Tudorica LA, et al. Intratumor mapping of intracellular water lifetime: metabolic images of breast cancer? *NMR Biomed*. 2014;27:760–773.
2. Bai R, Springer CS, Plenz D, Basser PJ. Fast, Na^+/K^+ pump driven, steady-state transcytolemmal water exchange found in neuronal tissue: a study of rat brain cortical cultures. *Magn Reson Med*. 2018;79:3207–3217.
3. Springer CS. Using ${}^{1}H_2O$ to measure and map sodium pump activity in vivo. *J Magn Reson*. 2018;291:110–126.
4. Bai R, Springer CS, Plenz D, Basser PJ. Brain active trans-membrane water cycling measured by MR is associated with neuronal activity. *Magn Reson Med*. 2019;81:1280–1295.
5. Ruggiero MR, Baroni S, Pezzana S, Ferrante G, Crich SG, Aime S. Evidence for the role of intracellular water lifetime as a tumor biomarker obtained by in vivo field-cycling relaxometry. *Angew Chem Int Ed Engl*. 2018;57:7468–7472.
6. Li LZ, Zhou R, Xu HN, et al. Quantitative magnetic resonance and optical imaging biomarkers of melanoma metastatic potential. *Proc Natl Acad Sci U S A*. 2009;106:6608–6613.
7. Li X, Priest RA, Woodward WJ, et al. Cell membrane water exchange effects in prostate DCE-MRI. *J Magn Reson*. 2012;218:77–85.

8. Li X, Rooney WD, Springer CS. A unified MRI pharmacokinetic theory for intravascular and extracellular contrast reagents. *Magn Reson Med*. 2005;54:1351–1359. [Erratum; 55, 1217 (2006)].
9. Zhang Y, Poirier-Quinot M, Springer CS, Balschi JA. Active trans-plasma membrane water cycling in yeast is revealed by NMR. *Biophys J*. 2011;101:2833–2842.
10. Ruggiero MR, Baroni S, Aime S, Crich SG. Relaxometric investigations addressing the determination of intracellular water lifetime: a novel tumor biomarker of general applicability. *Mol Phys*. 2018. https://doi.org/10.1080/00268976.2018.1527045
11. Rooney WD, Johnson G, Li X, et al. The magnetic field and tissue dependences of human brain longitudinal ^1H_2O relaxation in vivo. *Magn Reson Med*. 2007;57:308–318.
12. Rooney W, Sammi M, Grinstead J, et al. Contrast reagent detection sensitivity increases with B_0: 3 T and 7 T comparisons of the human head. In: Proceedings of the 21st Annual Meeting of ISMRM, Salt Lake City, Utah, 2013. Abstract 1224.
13. Avedano S, Botta M, Haigh JS, Longo DL, Woods M. Coupling fast water exchange to slow molecular tumbling in Gd^{3+} chelates: why faster is not always better. *Inorg Chem*. 2013;52:8436–8450.
14. Andrew ER, Bydder G, Griffiths J, Iles R, Styles P. Principles of magnetic resonance imaging. In: *Clinical Magnetic Resonance: Imaging and Spectroscopy*. Chichester: John Wiley & Sons; 1990:36.
15. Ball P. Water is an active matrix of life for cell and molecular biology. *Proc Natl Acad Sci U S A*. 2017;114:13327–13335.
16. Persson E, Halle B. Cell water dynamics on multiple time scales. *Proc Natl Acad Sci U S A*. 2008;105:6266–6271.
17. Li X, Cai Y, Moloney B, et al. Relative sensitivities of DCE-MRI pharmacokinetic parameters to arterial input function (AIF) scaling. *J Magn Reson*. 2016;269:104–112.
18. Landis CS, Li X, Telang FW, et al. Equilibrium transcytolemmal water exchange kinetics in skeletal muscle in vivo. *Magn Reson Med*. 1999;42:467–478.
19. Persson F, Halle B. Transient access to the protein interior: simulation versus NMR. *J Am Chem Soc*. 2013;135:8735–8748.
20. Sehy JV, Banks AA, Ackerman JJH, Neil JJ. Importance of intracellular water apparent diffusion to the measurement of membrane permeability. *Biophys J*. 2002;83:2856–2863.
21. Tzur A, Kafri R, LeBleu VS, Lahav G, Kirschner MW. Cell growth and size homeostasis in proliferating animal cells. *Science*. 2009;325:167–181.
22. McConnell HM. Reaction rates by nuclear magnetic resonance. *J Chem Phys*. 1958;28:430–431.
23. Woessner DE. Nuclear transfer effects in nuclear magnetic resonance pulse experiments. *J Chem Phys*. 1961;35:41–48.
24. Bai R, Springer CS, Basser PJ. The vanishing shutter-speed limit. In: Proceedings of the 25th Annual Meeting of ISMRM, Honolulu, Hawaii, 2017. Abstract 1918.
25. Labadie C, Lee J-H, Vétek G, Springer CS. Relaxographic imaging. *J Magn Reson B*. 1994;105:99–112.
26. Lee SK, Möβle M, Myers W, et al. SQUID-detected MRI at 132 μT with T_1–weighted contrast established at 10 μT to 300 mT. *Magn Reson Med*. 2005;53:9–14.
27. Landis CS, Li X, Telang FW, et al. Determination of the MRI contrast agent concentration time course in vivo following bolus injection: effect of equilibrium transcytolemmal water exchange. *Magn Reson Med*. 2000;44:563–574.
28. Coelho-Filho OR, Mongeon F-P, Mitchell R, et al. Role of transcytolemmal water-exchange in magnetic resonance measurements of diffuse myocardial fibrosis in hypertensive heart disease. *Circ Cardiovasc Imaging*. 2013;6:134–141.
29. Vétek G, Sammi MK, Lee J-H, Springer CS. Equilibrium exchange effects in relaxographic imaging: quantitative analysis. In: Proceedings of the 4th Annual Meeting of ISMRM, New York, New York, 1996. Abstract 1560.
30. Wilson GJ, Woods M, Springer CS, Bastawrous S, Bhargava P, Maki JH. Human whole-blood ^1H_2O longitudinal relaxation with normal and high-relaxivity contrast reagents: influence of trans-cell-membrane water exchange. *Magn Reson Med*. 2014;72:1746–1754.
31. Li X, Huang W, Morris EA, et al. Dynamic NMR effects in breast cancer dynamic-contrast-enhanced MRI. *Proc Natl Acad Sci U S A*. 2008;105:17937–17942.
32. Prantner AM, Bretthorst GL, Neil JJ, Garbow JR, Ackerman JJH. Magnetization transfer induced biexponential relaxation. *Magn Reson Med*. 2008;60:555–563.
33. Murase K. Generalized equation for describing the magnetization in spoiled gradient-echo imaging. *Magn Reson Imaging*. 2011;29:723–730.
34. Springer F, Steidle G, Martirosian P, Claussen CD, Schick F. Effects of in-pulse transverse relaxation in 3D ultrashort echo time sequences: analytical derivation, comparison to numerical simulation and experimental application at 3 T. *J Magn Reson*. 2010;206:88–96.
35. Ou X, Gochberg DF. MT effects and T_1 quantification in single-slice spoiled gradient echo imaging. *Magn Reson Med*. 2008;59:835–845.
36. Buckley DL. Shutter-speed dynamic contrast-enhanced MRI: is it fit for purpose? *Magn Reson Med*. 2019;81:976–988.
37. Wilson GJ, Springer CS, Bastawrous S, Maki JH. Human whole blood ^1H_2O transverse relaxation with gadolinium-based contrast reagents: magnetic susceptibility and transmembrane water exchange. *Magn Reson Med*. 2017;77:2015–2027.
38. Lee J-H, Springer CS. The effects of equilibrium exchange on diffusion-weighted NMR signals: the diffusigraphic 'shutter-speed'. *Magn Reson Med*. 2003;49:450–458. [Erratum; 51, 222 (2004)].
39. Mulkern RV, Balasubramanian M, Maier SE. On the perils of multiexponential fitting of diffusion MR data. *J Magn Reson Imaging*. 2017;45:1545–1547.
40. Zhang Y, Poirer-Quinot M, Springer CS, Balschi JA. Discrimination of intra- and extracellular $^{23}Na^+$ signals in yeast cell suspensions using longitudinal magnetic resonance relaxography. *J Magn Reson*. 2010;205:28–37.
41. Hürlimann MD, Helmer KG, de Swiet TM, Sen PN, Sotak CH. Spin echoes in a constant gradient and in the presence of simple restriction. *J Magn Reson A*. 1995;113:260–264.
42. Sukstanskii AL, Ackerman JJH, Yablonskiy DA. Effects of barrier-induced nuclear spin magnetization inhomogeneities on diffusion-attenuated MR signal. *Magn Reson Med*. 2003;50:735–742.
43. Zhang Y, Balschi JA. Water exchange kinetics in the isolated heart with Na^+/K^+ ATPase activity: potentially high spatiotemporal resolution in vivo MR access to cellular metabolic activity. In: Proceedings of the 21st Annual Meeting of ISMRM, Salt Lake City, Utah, 2013. Abstract 4045.
44. Koch CJ, Jenkins WT, Jenkins KW, et al. Mechanisms of blood flow and hypoxia production in rat 9L-epigastric tumors. *Tumor Microenviron Ther*. 2013;1:1–13.
45. Bailey C, Giles A, Czarnota GJ, Stanisz GJ. Detection of apoptotic cell death in vitro in the presence of Gd-DTPA-BMA. *Magn Reson Med*. 2009;62:46–55.

46. Bailey C, Moosvi F, Stanisz GJ. Mapping water exchange rates in rat tumor xenografts using the late-stage uptake following the bolus injections of contrast agent. *Magn Reson Med*. 2014;71:1874–1887.
47. Mehrabian H, Desmond KL, Chavez S, et al. Water exchange rate constant as a biomarker of treatment efficacy in patients with brain metastases undergoing stereotactic radiosurgery. *Int J Radiat Oncol Biol Phys*. 2017;98:47–55.
48. Nath K, Paudyal R, Nelson DS, et al. Acute changes in cellular-interstitial water exchange rate in DB-1 melanoma xeongrafts after lonidamine admistration as a marker of tumor energetics and ion transport. In: Proceedings of the 22nd Annual Meeting of ISMRM, Milan, Italy, 2014. Abstract 2757.
49. Guo L, Shestov AA, Worth AJ, et al. Inhibition of mitochondrial complex II by the anticancer agent lonidamine. *J Biol Chem*. 2016;291:42–57.
50. Tudorica A, Oh KY, Chui SY-C, et al. prediction and evaluation of breast cancer response to neoadjuvant chemotherapy using quantitative DCE-MRI. *Transl Oncol*. 2015;9:8–17.
51. Springer CS, Li X, Jayatilake ML, et al. Metabolic imaging of early tumor therapy. In: Proceedings of the 23rd Annual Meeting of ISMRM, Toronto, Canada, 2015. Abstract 3860.
52. Rooney WD, Li X, Sammi MK, Bourdette DN, Neuwelt EA, Springer CS. Mapping human brain capillary water lifetime: high-resolution metabolic neuroimaging. *NMR Biomed*. 2015;28:607–623.
53. Chawla S, Loevner LA, Kim SG, et al. Dynamic contrast-enhanced MRI-derived intracellular water lifetime (τ_i): a prognostic marker for patients with head and neck squamous cell carcinomas. *Am J Neuroradiol*. 2018;39:138–144.
54. Inglese M, Cavaliere C, Monti S, et al. A multi-parametric PET/MRI study of breast cancer: evaluation of DCE-MRI pharmacokinetic models and correlation with diffusion and functional parameters. *NMR Biomed*. 2018;e4026.
55. Damadian R. Tumor detection by nuclear magnetic resonance. *Science*. 1971;171:1151–1153.
56. Lauterbur PC. One path out of many – how MRI actually began. *Encly NMR*. 1996;1:445–449.
57. Lauterbur PC. Image formation by induced local interactions: examples employing nuclear magnetic resonance. *Nature*. 1973;242:190–191.
58. Budinger TF, Bird MD, Frydman L, et al. Toward 20 magnetic resonance for human brain studies: opportunities for discovery and neuroscience rationale. *MAGMA*. 2016;29:617–639.
59. Ross PJ, Broche LM, Lurie DJ. Rapid field-cycling MRI using fast spin-echo. *Magn Reson Med*. 2015;73:1120–1124.
60. McDaniel PC, Cooley CZ, Stockmann JP, Wald LL. A 6.3 kg single-sided magnet for 3D, point-of-care brain imaging. In: Proceedings of the 26th Annual Meeting of ISMRM, Paris, France, 2018. Abstract 943.

How to cite this article: Li X, Mangia S, Lee J-H, Bai R, Springer CS Jr. NMR shutter-speed elucidates apparent population inversion of ^1H_2O signals due to active transmembrane water cycling. *Magn Reson Med*. 2019;82:411–424. https://doi.org/10.1002/mrm.27725

APPENDIX: ACRONYMS AND SYMBOLS

APE	apparent population equality
API	apparent population inversion
ATP	adenosine triphosphate
⟨A/V⟩	mean cell area/volume ratio
AWC	active water cycling
α	read pulse flip angle
$\mathbf{B}_0$	main magnetic field
BMW	Bloch-McConnell-Woessner
CA	contrast agent
CA_i	intracellular CA
CA_o	extracellular CA
$[CA_o]$	CA_o concentration
DCE	dynamic-contrast-enhanced
DWI	diffusion-weighted imaging
ECF	tissue extracellular volume fraction
FXL	fast-exchange limit
FXR	fast-exchange-regime
f_M	tissue macromolecular volume fraction
H_2O_{bu}	buried water
H_2O_i	intracellular water
H_2O_o	extracellular water
$[H_2O_i]$	H_2O_i concentration
^1H_2O	water proton MR signal
$^1H_2O_i$	H_2O_i MR signal
$^1H_2O_o$	H_2O_o MR signal
k	steady-state water exchange rate constant
k_{io}	water efflux k ($1/\tau_i$)
$k_{io}(a)$	active k_{io} contribution
$k_{io}(p)$	passive k_{io} contribution
k_{oi}	water influx k
K-Ras	Kirsten rat sarcoma virus oncogene
κ_1	longitudinal MR shutter-speed (SS)
LSS	large SS condition (formerly, SXR)
LSSL	large SS limit (formerly, SXL)
$^cMR_{NKA}$	cellular NKA metabolic rate
MW	molecular mass
NKA	Na^+,K^+-ATPase (sodium pump)
NXL	no-exchange-limit
ν_L	Larmor frequency (often ν_0)
ν_{Li}	$^1H_2O_i$ ν_L
ν_{Lo}	$^1H_2O_o$ ν_L
p	tissue water mole fraction (“population”)
p_i	intrinsic H_2O_i p
p_o	intrinsic H_2O_o p
p′	apparent p
p'_{fast}	fast-relaxing component p′ (formerly, a_S)

p'_i	H_2O_i p'
p'_{slow}	slow-relaxing component p' (formerly, a_L)
p'_o	H_2O_o p'
PMA1	plasma membrane H^+-ATPase
P_W	membrane water permeability coefficient
$P_W(p)$	passive P_W
R_1	longitudinal relaxation rate constant
$R_{1,cross}$	$= R_{1i} = R_{1o}$
R_{1i}	intrinsic $^1H_2O_i$ R_1
R_{1H2O}	pure water R_1
R_{1o}	intrinsic $^1H_2O_o$ R_1
R_{1o0}	R_{1o} in the absence of CA_o
R'_1	apparent, approximate single R_1 value
$R'_{1,fast}$	fast-relaxing component R'_1 (formerly, R_{1S})
R'_{1i}	apparent R_{1i}
R'_{1o}	apparent R_{1o}
$R'_{1,slow}$	slow-relaxing component R'_1 (formerly, R_{1L})
R_2	transverse relaxation rate constant
R'_2	apparent R_2
$R'_{2,fast}$	fast-relaxing component R'_2
$R'_{2,slow}$	slow-relaxing component R'_2
RHS	right-hand side
r_1	longitudinal relaxivity
r_{1M}	macromolecular r_1
r_{1o}	CA_o r_1
ρ	cell (number) density
S	tissue ^1H_2O signal strength
S_0	Boltzmann S
$\mathbf{S}'_{fast}$	apparent fast-relaxing saturation factor
$\mathbf{S}'_{slow}$	apparent slow-relaxing saturation factor
SS	shutter-speed (κ_1)
SSS	small SS condition (formerly, FXR)
SXL	slow-exchange-limit
SXR	slow-exchange-regime
TE	pulse sequence magnetization echo time
TR	pulse sequence repetition time
T_1	longitudinal relaxation time constant
T_{1o}	intrinsic $^1H_2O_o$ T_1
τ_i	mean H_2O_i molecule lifetime ($1/k_{io}$)
τ_r	molecular rotational correlation time
$\langle V \rangle$	mean cell volume
VSS	vanished SS condition (formerly, FXL)
v	tissue volume fraction
v_i	intracellular v
v_o	extracellular v (formerly, ECF)
2SX	two-site-exchange